

NEAR-INFRARED EMISSION-LINE IMAGES OF THREE HERBIG-HARO OBJECTS¹

KARL R. STAPELFELDT,² CHARLES A. BEICHMAN,^{2,3} J. JEFF HESTER,^{2,3}
 NICHOLAS Z. SCOVILLE,² AND THOMAS N. GAUTIER III^{2,3}

Received 1989 September 11; accepted 1990 August 10

ABSTRACT

HH 7–11, HH 12, and HH 34 have been observed with an infrared array camera using nine narrow-band filters. We report the first detection of the $1.64\ \mu\text{m}$ line of [Fe II] in all three Herbig-Haro objects, including the HH 34 jet. Vibrational lines of H_2 were imaged in HH 7–11 and HH 12, but were not detected in HH 34. Brackett- γ emission was not detected in any of the HH objects. The infrared results are compared with optical [S II] images. No new emission-line regions are revealed in the infrared data, suggesting that extinction plays little role in determining the optical appearance of these HH objects.

The spatial distribution of [Fe II] emission is generally similar to the distribution of $6717\ \text{\AA}$ [S II] emission. The [Fe II]/[S II] ratio is very different in HH 12E, where the value is down by a factor of 7 relative to the rest of HH 12. At this location we suggest that the cooling and recombining flow behind the shock is disrupted before the [Fe II] emission zone can form.

In HH 7–11 and HH 12, H_2 emission peaks are nearly always accompanied by [Fe II] and [S II] emission. In three locations (western HH 7; eastern HH 12C and HH 12D) ionized gas peaks occur without H_2 counterparts; these locations all occur $2''$ – $5''$ upstream of H_2 emission. We identify these peaks without H_2 as shocked jet/wind material, displaced upstream from the H_2 emission at the flow terminus. We suggest that the geometry of a flow obstacle controls whether or not the standoff distance between the molecular and ionized gas shocks is large enough to be observable.

No infrared continuum emission was detected from any of the HH objects, indicating that none contain embedded stars. An infrared reflection nebula has been detected to the north of the HH 34 exciting star.

Subject headings: infrared: sources — nebulae: individual (HH 7–11, HH 12, HH 34) — shock waves — stars: pre-main-sequence

1. INTRODUCTION

Herbig-Haro objects mark the locations where energetic winds from young stellar objects confront the dense quiescent gas of surrounding molecular clouds. The shock wave nature of HH objects, their association with bipolar molecular outflows, their often large proper motion, and their proximity to highly reddened young stars has been clear for several years (see Schwartz 1983 for a review). HH objects exhibit a wide variation in morphology (see Strom *et al.* 1986); for this reason, their specific shock geometries have been a matter of some debate. Discrete stellar mass ejections (“bullets”; Norman and Silk 1979) and ambient cloudlets in a supersonic stellar wind (Schwartz 1978) are models that have been proposed. Recently, many HH objects have been interpreted as collimated optical jets and jet working surfaces (Mundt, Brugel, and Bührke 1987).

It is clear that there is much to be gained by studying HH objects at near-infrared wavelengths. The exciting stars of HH objects can usually be located only by infrared mapping since they are highly obscured at optical wavelengths. Extinction may also bias our view of the HH objects themselves; there are fewer known redshifted objects, i.e., those moving deeper into the host clouds. In addition, the near-infrared includes a unique spectroscopic tracer: the H_2 vibrational emission pro-

duced by shock-heated molecular gas. Using new infrared array detectors, it is now possible to obtain high-resolution images comparable to those at optical wavelengths. This new capability offers the opportunity for a detailed comparison of the molecular, atomic, and ionized gas tracers of the Herbig-Haro object shock fronts. The spatial relationship between the molecular and atomic emission should be indicative of the shock type and geometry within an individual HH object.

In this paper, we present flux-calibrated imagery in five emission-line and four narrow-band continuum filters for three classical HH objects. The emission lines studied {[Fe II], Br γ , and $\text{H}_2\ v = 1-0\ S(1)$, $1-0\ Q(3)$, and $2-1\ S(1)$ } were chosen for imaging in order to selectively probe low-excitation ionized gas ([Fe II]), high-excitation ionized gas (Br γ), and the hot molecular gas shock fronts (H_2). Graham, Wright, and Longmore (1987) have detected the $1.64\ \mu\text{m}$ [Fe II] line in the spectrum of the supernova remnant IC 443 and suggested that it could be a useful tracer of ionized gas in low-velocity shocks. Furthermore, Hollenbach and McKee (1989) have carried out detailed modeling of the near-infrared emission line spectra of J shocks in molecular clouds and suggest that [Fe II] emission should be present in HH objects. Vibrational H_2 emission has been detected in many HH objects (e.g., Schwartz, Cohen, and Williams 1987). Near-infrared imaging of H_2 emission has been carried out by several workers: Schwartz *et al.* 1988 (HH 43); Hartigan, Curiel, and Raymond 1989 (HH 7–11); Lane 1989 (Cepheus A, HH 24, HH 33–40, RNO 43N); and Garden, Russell, and Burton 1990 (HH 7–11, HH 12). The current contribution improves on the previous H_2 imaging in several respects. Narrow-band continuum images were obtained to

¹ Observations were obtained in part with the Palomar 60 inch (1.5 m) telescope, which is operated jointly by the California Institute of Technology and the Carnegie Institution of Washington.

² Palomar Observatory, California Institute of Technology.

³ Infrared Processing and Analysis Center, Jet Propulsion Laboratory, California Institute of Technology.

discriminate between line and continuum sources. Imaging was carried out in three H_2 lines, constraining the extinction and excitation conditions. All of the data has been flux-calibrated; and last, careful registration of the infrared images with optical images has been done.

II. OBSERVATIONS AND REDUCTION

The observations were carried out with the new Prime Focus infrared camera (Beichman *et al.* 1991) on the 5 m Hale telescope during four observing runs from 1988 September to 1989 March. The detector was a Rockwell 128×128 HgCdTe array with reticon readout, 40% quantum efficiency from 1.6 μm to 2.45 μm , read noise of 1200 electrons, and a linear well depth of 6×10^5 electrons. The camera optics provide the detector with a $98''$ field of view and $0''.765$ pixels. The emission-line images were made with 1% wide filters at 1.64 μm ([Fe II]), 2.12 μm [H_2 1–0 S(1)], 2.16 μm (Br γ), 2.24 μm [H_2 2–1 S(1)], and 2.42 μm [H_2 1–0 Q(3)]. Narrow-band filters that avoid strong emission lines were used to measure the continuum at 1.57, 2.08, 2.19 and 2.38 μm . Broad-band J , H , K filter images were also obtained for reference.

The observing sequence consisted of taking object, bias, sky, and dark frames, and observations of standard stars. Exposure times in the narrow-band filters were typically 500 s; Q(3) exposures were limited to 150 s by sky emission. All images were bias-subtracted, dark-subtracted, and flattened. Flat-field frames were generated by taking the median of a number of normalized sky frames. The data were processed to remove low-level low spatial frequency noise present in the serial data stream from the camera. In each frame, "hot pixel" data values were replaced by a local median calculated over a 3×3 pixel box. Final images were constructed by co-adding several individual frames. The $98''$ field of view was large enough to include the full areas of HH 7–11 and HH 12; however, three fields were required to cover HH 34. The narrow-band images were flux-calibrated using tracings of the cold filter transmission functions and observations of standard A stars from the list of Elias *et al.* (1982). Our 3σ limiting surface brightness corresponds to about 4×10^{-5} ergs s^{-1} cm^{-2} sr^{-1} in the emission line filters, and 0.04 Jy pixel $^{-1}$ in the continuum.

Calibration of the Q(3) line is more complex than for the other lines due to emission in the bandpass from the Q(1) and Q(2) lines as well as atmospheric extinction due to water vapor. The contribution of Q(1) and Q(2) can be estimated in LTE using H_2 A -values from Turner, Kirby-Docken, and Dalgarno (1977). The ratios are $Q(1)/Q(3) = 1$, and $Q(2)/Q(3) = \frac{1}{3}$ with only 10% variation from $1500 < T < 2600$ K. After adjustment for filter transmission differences, we find that Q(3) makes up 49% of the line flux observed in the 2.42 μm filter. The atmospheric absorption correction is more difficult: narrow H_2O lines are located 25 km s^{-1} to the red of both the Q(3) and Q(1) rest wavelengths (Delbouille *et al.* 1981). The atmospheric extinction in the lines was estimated from Q(3) observations of HH 2 ($V_{\text{rad}} = 25$ km s^{-1} ; Zinnecker *et al.* 1989) at different airmasses. We found a Q(3) extinction of 0.2 mag airmass $^{-1}$. We estimate the two corrections discussed above may introduce a 30% systematic uncertainty in the derived Q(3) fluxes. The usefulness of Q(3) for revealing reddening variations within a field is unaffected by this uncertainty.

The optical [S II] frames were obtained during 1988 November using a TI 800×800 CCD at the Cassegrain focus of the Palomar 60 inch telescope. In the direct imaging mode with 2×2 on-chip binning the image scale was $0''.49$ pixel $^{-1}$. The

[S II] filter was centered on the 6717 Å line and had a FWHM of 10 Å. $H\alpha$ frames (not presented here) were also obtained for reference. The CCD images were bias-subtracted using the overscan of the serial registers and flattened against dome flats. Subimages were extracted to correspond to the infrared camera field size and aligned with the infrared images by applying a scale change and a small rotation. The optical and infrared images were then registered to a common origin using a reference star in the field.

The scale and rotation parameters were determined using a two-step procedure. First, scale and rotation were determined astrometrically: for the infrared camera we used 19 Trapezium stars and positions from Herbig and Terndrup (1986); for the CCD images we used five HH 34 field stars and positions from Strom *et al.* (1986). The astrometric method yielded a scale ratio of 1.556 ± 0.009 and a rotation angle of $0^\circ.5 \pm 0^\circ.4$. These results were then checked against K band and $H\alpha$ images of HH 12; a pair of stars separated by $67''$ is visible in both frames. The vector between these two stars was measured in both the IR and CCD images, yielding an improved rotation angle of $0^\circ.2 \pm 0^\circ.2$.

III. RESULTS AND DISCUSSION

Images in [Fe II], H_2 , narrow-band infrared continuum, and optical [S II] were assembled together in Figure 1 (Plate 14) for HH 7–11 and in Figure 5 (Plate 15) for HH 12. For HH 34, broad-band J , H , K , [Fe II], and [S II] images were assembled into Figure 7 (Plate 16). Continuum emission from the HH objects was found to be negligible; we therefore chose not to subtract the continuum from the line images because of the added noise which would result. Individual objects in the fields are identified in the lower right panels of Figures 1, 5, and 7. The area of each object used for flux measurements in Table 1 was defined as the contiguous region of pixels where individual pixel values exceeded 3 times the single-pixel noise σ measured in an empty area of each image. This aperture size determination was performed using both the [Fe II] and H_2 images; for each object, the larger aperture of the two was then chosen for all the line photometry. Intensity upper limits are calculated as 3σ , while flux upper limits are calculated as $3\sigma N^{1/2}$ (N is the number of pixels in the aperture). The derived peak intensity of an object was found by a weighted average of the brightest pixel with its four nearest neighbors.

A detailed justification for the identification of 1.64 μm emission as [Fe II] emission is given at the end of § III.

a) HH 7–11

HH 7–11 is a nearly colinear system of optical emission knots in the L1450 molecular cloud near NGC 1333 (see Strom *et al.* 1986). The estimated distance is 350 pc. The complex lies in the blue lobe of an outflow observed in 2.6 mm CO emission (Snell and Edwards 1981). A massive neutral atomic wind apparently drives this CO outflow (Lizano *et al.* 1988). The optical ionized gas emission lines are centered at LSR radial velocities of -200 to -40 km s^{-1} (Stapelfeldt, Trauger, and Scoville 1991; Solf and Böhm 1987). The H_2 1–0 S(1) emission line is centered at much lower radial velocities of -60 to 0 km s^{-1} (Carr 1990; Zinnecker *et al.* 1989), a fact important to shock models of the region. Rudolph and Welch (1989) have found zero velocity HCO^+ emission regions offset downstream of HH 8, 9, 10, and 11; they interpret this as evidence of shocked ambient cloudlets. The source of the outflow and

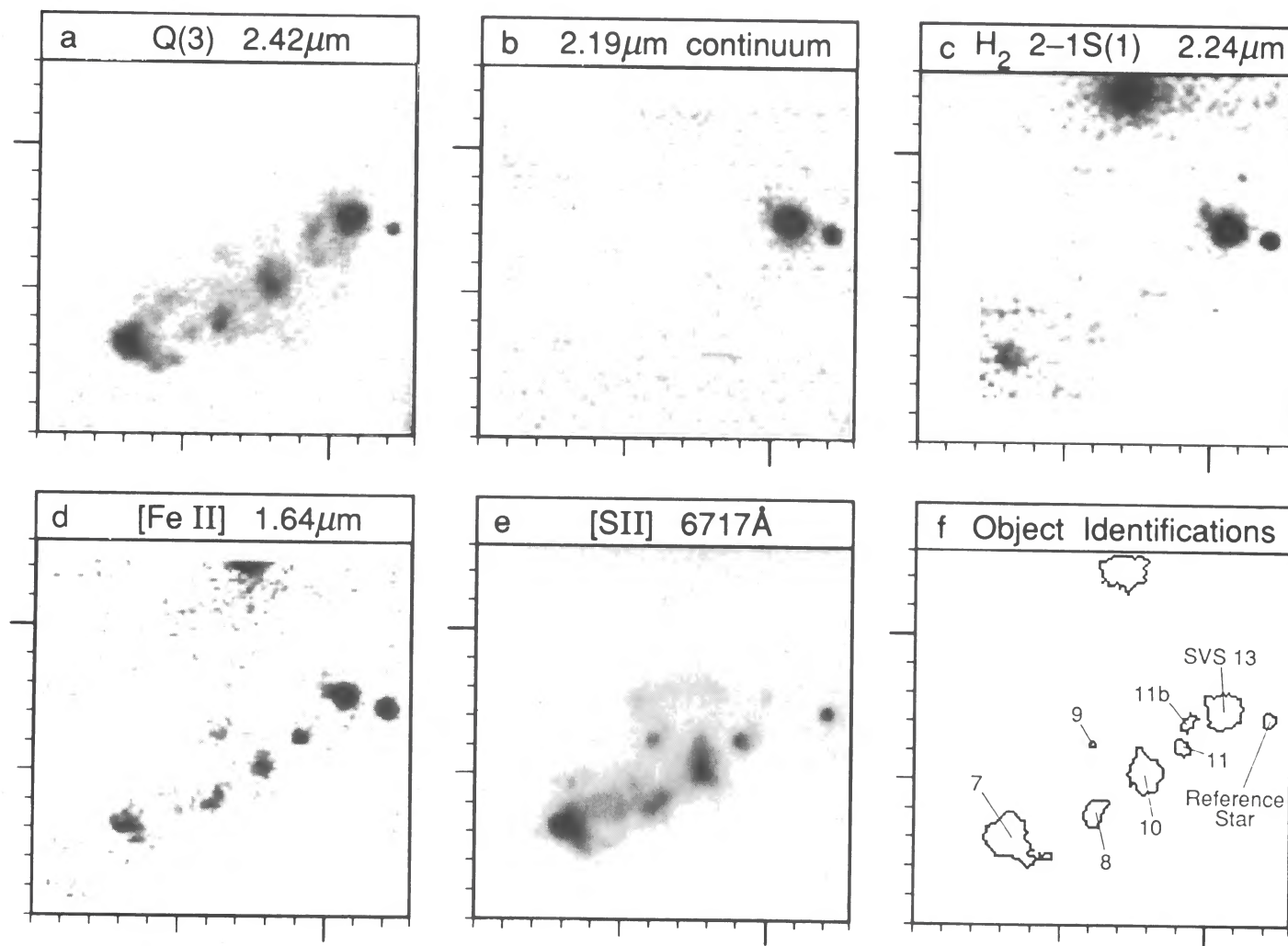


FIG. 1.—Images of HH 7–11. Figs. 1a–1d are infrared images, Fig. 1e is the optical image, and Fig. 1f identifies the objects whose photometry is given in Table 1. Tick marks are given in 10 pixel (7.65) increments. The field of view is 98 arcsec².

STAPELFELDT et al. (see 371, 227)

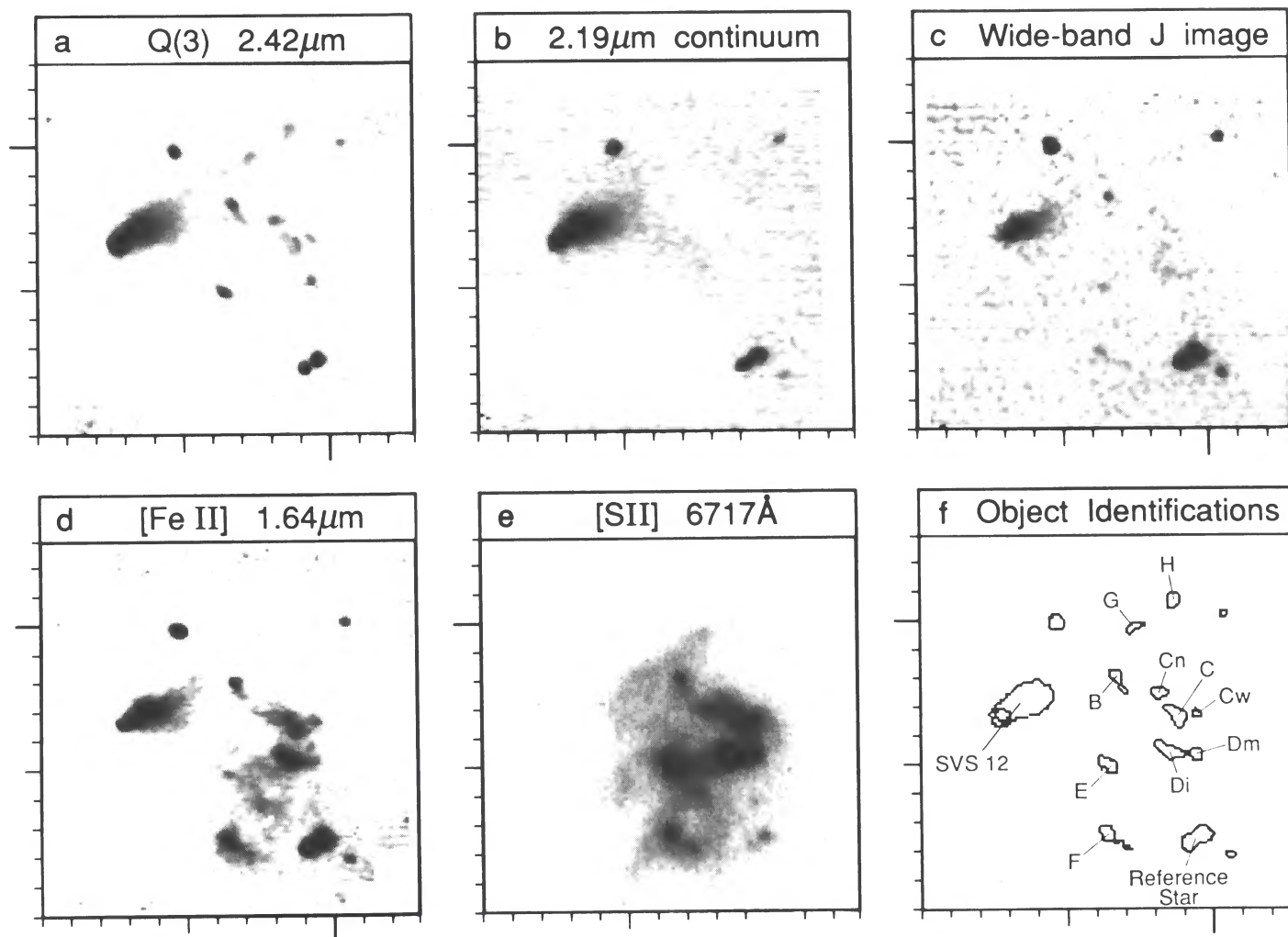


FIG. 5.—Images of HH 12. Figs. 5a–5d are infrared images, Fig. 5e is the optical image, and Fig. 5f identifies the objects discussed in the text. Tick marks are given in 10 pixel ($7''.65$) increments. The field of view is 98 arcsec^2 .

STAPELFELDT et al. (see 371, 227)

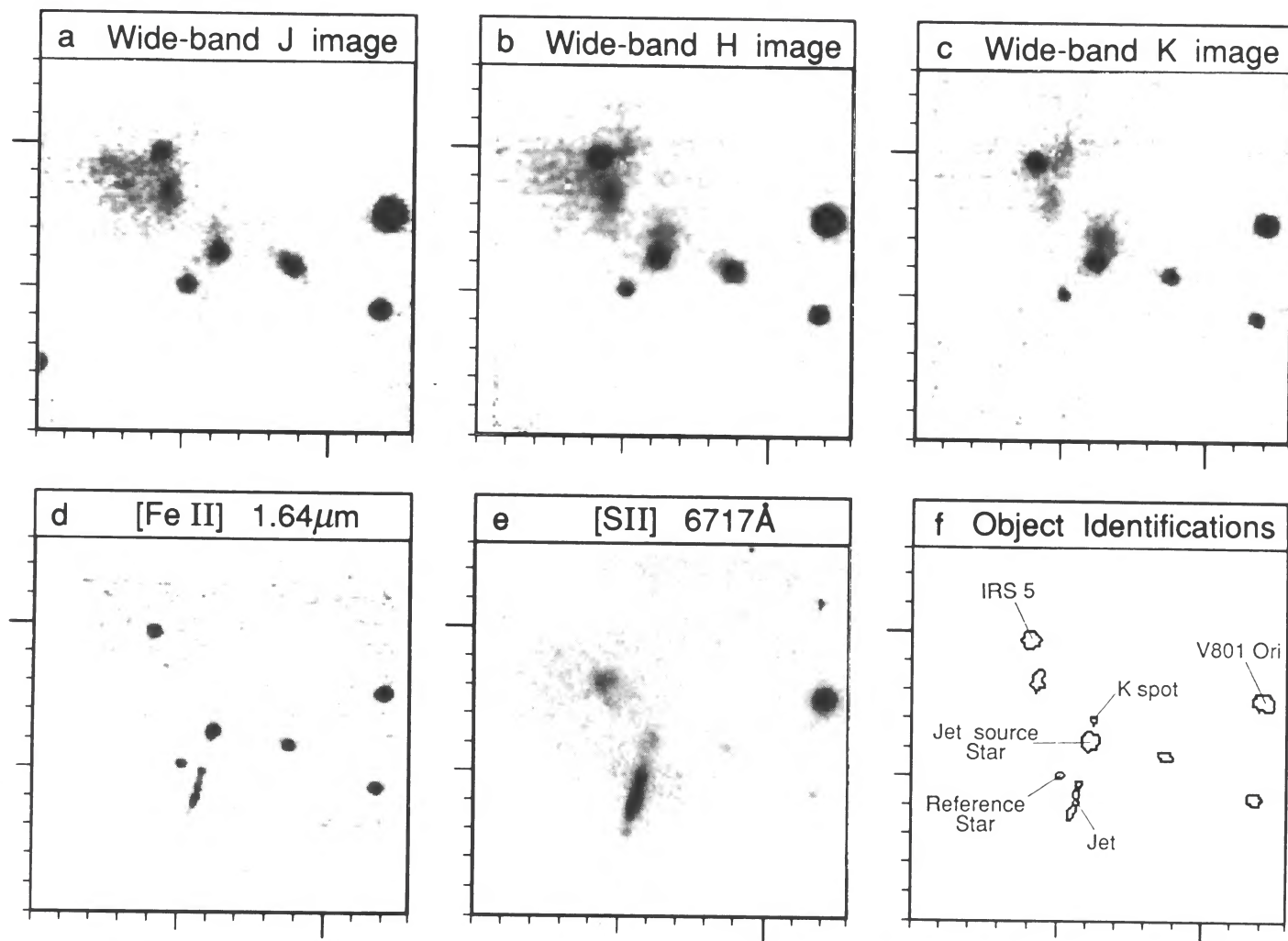


FIG. 7.—Images of the HH 34 jet field. Figs 7a–7d are infrared images, Fig. 7e is the optical image, and Fig. 7f identifies the objects discussed in the text. Tick marks are given in 10 pixel (7.65) increments. The field of view is 98 arcsec².

STAPELFELDT et al. (see 371, 227)

TABLE 1
HH OBJECT FLUXES AND PEAK INTENSITIES

| OBJECT | APERTURE SIZE (arcsec ²) | [Fe II] (1.644 μ m) | H ₂ | | |
|-----------|--------------------------------------------|----------------------------|-----------------------------|-----------------------------|-----------------------------|
| | | | 1-0 S(1) (2.122 μ m) | 2-1 S(1) (2.248 μ m) | 1-0 Q(3) (2.424 μ m) |
| HH 7 | 134 | 10.3 (0.5) 0.9 (0.1) | 66.6 (3.0) 5.6 (0.2) | 5.9 (1.5) 1.1 (0.2) | 65. (17.) 5.3 (0.1) |
| HH 8 | 39 | 3.4 (0.3) 0.6 (0.1) | 12.5 (0.8) 3.0 (0.2) | 1.1 (0.3) 0.4 (0.2) | 12.6 (3.3) 2.7 (0.1) |
| HH 8b | 6 | 0.3 (0.1) 0.3 (0.1) | 1.1 (0.2) 0.9 (0.2) | <0.5 <0.5 | 1.3 (0.4) 0.9 (0.1) |
| HH 9 | 4 | 0.3 (0.1) 0.4 (0.1) | 0.5 (0.1) 0.7 (0.2) | <0.6 <0.5 | 0.4 (0.1) 0.4 (0.1) |
| HH 10 | 81 | 5.2 (0.4) 0.6 (0.1) | 22.9 (1.4) 2.4 (0.2) | 1.5 (0.9) 0.3 (0.2) | 25.5 (6.8) 2.5 (0.1) |
| HH 11 | 18 | 2.8 (0.2) 1.3 (0.1) | 1.8 (0.4) 0.6 (0.2) | <0.6 <0.5 | 1.9 (0.5) 0.8 (0.1) |
| HH 11b | 18 | <0.5 <0.3 | 4.0 (0.4) 1.1 (0.2) | <0.6 <0.5 | 4.4 (1.2) 1.3 (0.1) |
| HH 12B | 18 | 5.7 (0.2) 3.3 (0.2) | 3.6 (0.2) 4.5 (0.1) | <0.4 <0.5 | 4.0 (1.3) 2.2 (0.2) |
| HH 12C | 15 | 3.7 (0.2) 1.0 (0.2) | 2.2 (0.2) 0.8 (0.1) | <0.5 <0.5 | 2.2 (0.7) 0.6 (0.2) |
| HH 12Cn | 15 | 0.5 (0.1) 0.3 (0.2) | 2.7 (0.2) 1.6 (0.1) | <0.4 <0.5 | 2.2 (0.7) 1.0 (0.2) |
| HH 12Cw | 3 | 0.6 (0.1) 0.9 (0.2) | <0.3 <0.3 | <0.3 <0.5 | <0.2 <0.5 |
| HH 12Di | 29 | 6.5 (0.2) 1.4 (0.2) | <0.6 <0.3 | <0.5 <0.5 | <0.3 <0.5 |
| HH 12Dm | 13 | 1.5 (0.1) 0.9 (0.2) | 2.9 (0.2) 2.3 (0.1) | <0.3 <0.5 | 2.6 (0.6) 1.3 (0.2) |
| HH 12E | 19 | 1.0 (0.1) 0.8 (0.2) | 11.2 (0.5) 6.6 (0.1) | 0.5 (0.1) 0.4 (0.2) | 6.1 (1.9) 2.9 (0.2) |
| HH 12F | 23 | 6.5 (0.2) 2.3 (0.2) | <0.5 <0.3 | <0.4 <0.5 | <0.4 <0.5 |
| HH 12G | 12 | 0.9 (0.1) 0.6 (0.2) | 1.9 (0.2) 1.1 (0.1) | <0.3 <0.5 | 1.3 (0.4) 0.7 (0.2) |
| HH 12H | 15 | <0.3 <0.5 | 2.1 (0.2) 1.2 (0.1) | <0.3 <0.5 | 1.6 (0.5) 0.8 (0.2) |
| HH 34 jet | 23 | 4.0 (0.2) 1.1 (0.1) | <0.3 <0.6 | | <0.3 <0.4 |
| HH 34 S | 43 | 2.9 (0.2) 0.4 (0.1) | <0.7 <0.7 | | <0.4 <0.4 |
| HH 34 N | 43 | <0.4 <0.6 | <0.5 <0.6 | | <0.8 <0.4 |

NOTES.—(1) The apertures employed are outlined in Figs. 1*f*, 5*f*, and 7*f*. (2) Flux units are 10^{-14} ergs $s^{-1} cm^{-2}$. (3) Intensity units are 10^{-4} ergs $s^{-1} cm^{-2} sr^{-1}$. (4) Uncertainties given in parentheses; ... indicates no data taken. (5) The Q(3) values quoted here are corrected for Q(1) contamination.

exciting star of the HH emission is presumed to be the obscured star SVS 13.

None of the HH objects are evident in the 2.19 μ m continuum image (Fig. 1*b*). Continuum contamination is therefore insignificant in the line images of HH 7–11. SVS 13, the exciting star of the outflow, is the bright point source toward the upper right of Figure 1*b*.

i) [Fe II]

All of the optical HH objects are visible in the 1.64 μ m [Fe II] line (Fig. 1*d*). No optically invisible emission line regions are revealed in [Fe II]; from this we conclude that extinction has not strongly affected the optical appearance of the HH objects. The [Fe II] emission is spatially coincident with the optical [S II] emission except in HH 9, which appears extended 2" further upstream (closer to SVS 13) in [Fe II]. A knot of [Fe II] emission is seen adjacent to SVS 13, extending 4" to the ENE. Faint [S II] emission (Fig. 1*e*) is also seen in this

knot, suggesting that the obscuring dust near the star does not extend over this knot of gas. HH 11 shows the highest [Fe II] surface brightness in this system.

ii) H₂

The Q(3) image (Fig. 1*a*) shows the most intense H₂ emission in HH 7; HH 8 and 10 are moderately bright; HH 9 is faintly visible; and no H₂ emission is associated with the optical peak of HH 11. Two knots of Q(3) emission are present 3" west and 7" north of HH 11's optical position; these have no counterparts in the ionized gas. The H₂ peak to the north of HH 11, which we refer to as HH 11b, actually shows a better positional correspondence to Rudolph and Welch's HH 11 HCO⁺ peak than HH 11 itself. There is also low-intensity H₂ emission coincident with the western edges of HH 11. Last, note the diffuse H₂ emission apparently filling the outflow cavity between SVS 13 and the flow terminus at HH 7.

The 1-0 S(1) line image (not shown here) is virtually identical to the Q(3) image. Since these lines originate from the same

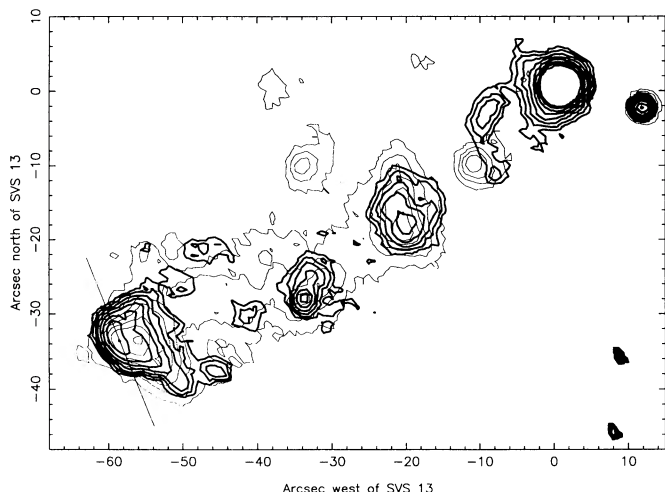


FIG. 2.—An overlay of two contour plots of the emission from HH 7–11. The dark contours represent H_2 $Q(3)$ emission; the light contours represent the 6717 \AA $[\text{S II}]$ emission. The contour interval is a factor of $\sqrt{2}$. The solid line through the head of HH 7 shows the path of the slit used to make the intensity plots in Fig. 3.

upper state, their similar distributions imply that the foreground extinction is relatively uniform. The $1-0 \text{ S}(1)$ flux we derive for HH 7 agrees very well with the value found by Hartigan, Curiel, and Raymond (1989) in a $12''$ aperture. The fluxes we obtained for HH 8 and HH 10 are smaller by 25% and 10%, respectively, probably because of our smaller apertures. The diffuse emission west of HH 8 has a typical intensity of $0.3 \text{ ergs s}^{-1} \text{ cm}^{-2} \text{ s}^{-1}$ in the $1-0 \text{ S}(1)$ line.

A contour map overlaying the H_2 and $[\text{S II}]$ emission morphology is shown in Figure 2. In HH 7, the H_2 morphology is significantly different from the $[\text{S II}]$ morphology. The brightest $[\text{S II}]$ emission originates in two peaks separated by $4''$ along the flow direction; only one peak is present in H_2 . The eastern $[\text{S II}]$ peak coincides (to the limits of our resolution and image registration) with the H_2 peak. However, there is a significant difference between the shape of the $[\text{S II}]$ peak and the shape of H_2 peak at this location: the H_2 emission is more extended perpendicular to the flow axis. This is shown quantitatively in Figure 3. A plot of intensity versus position along a line passing through the eastern peak at $\text{PA } 200^\circ$ reveals that the $[\text{S II}]$ peak $\text{FWHM} = 4.4''$, $[\text{Fe II}]$ peak $\text{FWHM} = 4.7''$, but the H_2 $\text{FWHM} = 6.2''$ (see Figs. 3a, 3b, 3c). These results are derived using a swath $4''$ wide and are therefore insensitive to infrared-optical image registration uncertainties. The western $[\text{S II}]$ peak has no H_2 counterpart; it does, however, correspond to the position of brightest $[\text{Fe II}]$ emission in HH 7.

Our results for HH 8 and HH 10 differ from those of Hartigan, Curiel, and Raymond (1989). Their Figure 2 depicts significant ($\approx 3''$ – $5''$) spatial offsets between the H_2 and $[\text{S II}]$ peaks in these objects. Our data do not confirm this: we find no offset at the southern peak of HH 8, and at most a $1''$ offset at northern HH 8 and HH 10. There is reason to believe our image registration is more reliable: the large field of view of our array covered all of HH 7–11 and a reference star, whereas HCR used a smaller array that demanded mosaicking without available reference stars. Furthermore, we find the infrared $[\text{Fe II}]$ peaks are coincident with the $[\text{S II}]$ peaks to within $1''$ in HH 8 and HH 10. This result, which is physically reasonable given the similar low-excitation characteristics of the two emis-

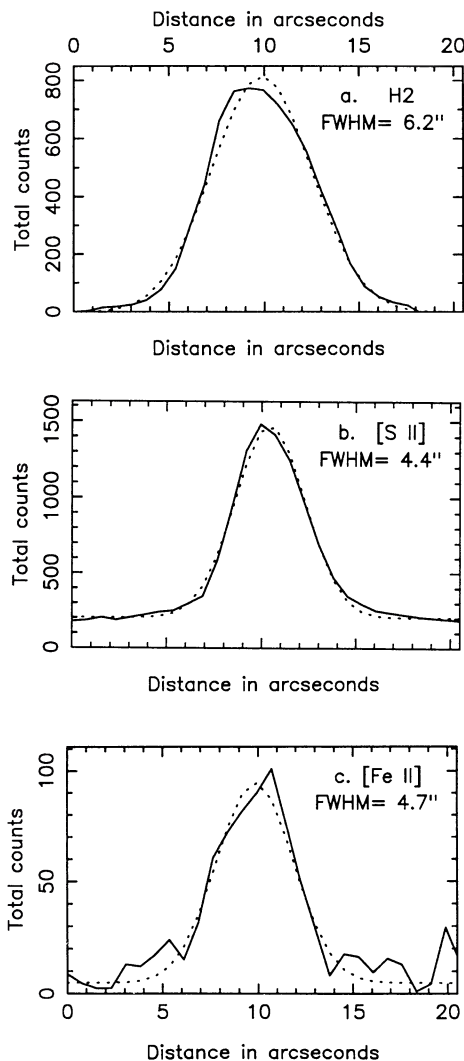


FIG. 3.—Intensity plots across the head of HH 7. Figs. 3a, 3b, and 3c are plots of intensity vs. position along a slit crossing the head of HH 7; the position and orientation of the slit are shown by the line in Fig. 2. The slit width is $4''$. The solid lines in Figs. 3a, 3b, and 3c represent the data; the dotted lines represent the best Gaussian least-squares fit to the data. Note the substantial difference in FWHM between the H_2 profile of Fig. 3a and the $[\text{S II}]$, $[\text{Fe II}]$ profiles of Figs. 3b and 3c.

sion lines, confirms that we have good optical-infrared image registration and thus that there are no H_2 – $[\text{S II}]$ offsets as large as $3''$ in HH 8 and HH 10.

The $2-1 \text{ S}(1)$ emission (see Fig. 1c) is clearly detected in two locations: at the brightest source of $v = 1-0$ emission (HH 7) and in an extension to the NE of SVS 13. The aperture photometry also shows $2-1 \text{ S}(1)$ emission in HH 8 and HH 10. Using the integrated flux values for HH 7 given in Table 1, we obtain a $v = 1-0/2-1$ ratio of 11. This is consistent with the results of Burton *et al.* (1988). The ratio at the emission peak is only 5, however, implying that the H_2 excitation conditions vary with position within HH 7. Models predict this line ratio to be dependent on the H_2 vibrational temperature, the ultraviolet radiation field, and the degree of molecule re-formation taking place (Hollenbach and McKee 1989). The knot of $2.24 \text{ }\mu\text{m}$ emission $7''$ NE of SVS 13 is enigmatic: it is displaced $2''$ north of an $[\text{S II}]$ – $[\text{Fe II}]$ peak; it is present in all of the $2 \text{ }\mu\text{m}$ images,

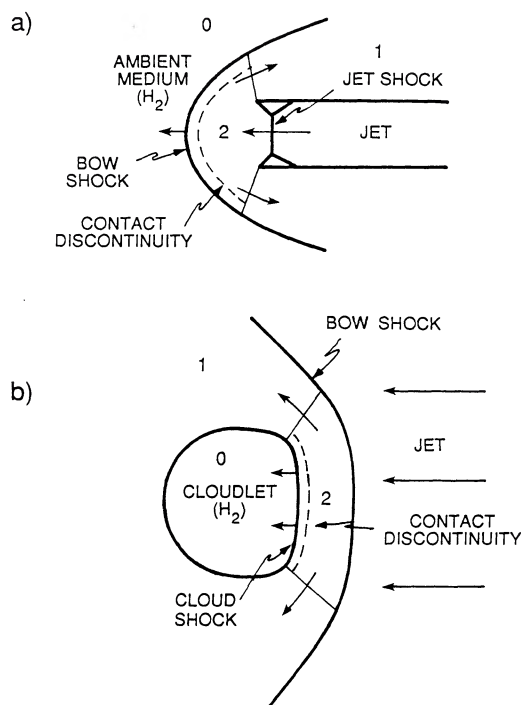


FIG. 4.—Schematic drawings of two possible types of HH objects: (a) the bow shock structure associated with the termination of the jet; and (b) the shock structure around a small clump of material being acted on by the jet.

including the continuum; and it is most prominent at the 2–1 $S(1)$ wavelength. If interpreted as H_2 line emission, the knot's $v = 2-1/1-0$ ratio is 2. This value is much higher than predicted by either the shock-excitation or ultraviolet fluorescence excitation mechanisms for H_2 .

iii) Interpretation

In a two-dimensional axisymmetric flow, a collimated stellar wind can produce two different shock geometries where the wind encounters an obstacle. Sketches of these two situations are shown in Figure 4. Figure 4a shows the shock structure associated with the termination of a jet; and Figure 4b shows the shock structure around a small clump of material being acted on by a jet. The most essential difference between these two situations is the relative sizes of the jet and the obstacle. In Figure 4a, depicting the flow terminus, the jet width is much less than the obstacle size; the ambient medium is very large. In Figure 4b, the jet width is much greater than the obstacle size. In both of these scenarios, two separate shock emission regions are expected: one from within shocked wind material, and a second from within shocked ambient material. A bow shock is present in both the jet terminus and shocked cloudlet scenarios, but with different characteristics in each. At the jet terminus (4a), a moving bow shock occurs in the ambient medium and is concave open toward the flow source. In the case of a cloudlet (4b), a stationary bow shock occurs in the wind material and is concave open away from the flow source. These figures are similar to the figures of Schwartz (1978), Hartigan (1989), and Zinnecker *et al.* (1989).

In the case of a neutral atomic wind flowing into a molecular medium (as Lizano *et al.* 1988 report is the case for HH 7–11), shocked wind material should not produce H_2 emission. Any H_2 emission detected in such a flow must originate in regions

of shocked ambient material. Therefore, for those HH objects where near-infrared H_2 emission is detected, it should be possible to infer whether a given HH emission knot is shocked ambient material or shocked wind material on the basis of the presence or absence of H_2 emission. This discriminant will prove useful in our discussion of the shock structure within HH objects.

A key difference between these two types of HH objects shown in Figure 4 should be the magnitude of the distance between the emission due to the shock in the wind material and the emission due to shock in the obstacle material. The displacement between these shocks reflects the amount of material which is present between them, which in turn is a function of the geometry of the obstacle. In the case of a small clump of material immersed in the flow (4b), there is little geometrical containment of the postshock gas. Shocked wind material is free to flow around the obstacle and continue downstream. Shocked ambient material at the surface of the clump may become entrained in the flow and carried away as well. Both of these mechanisms suggest that it is unlikely that a great deal of material will accumulate between the shock emission regions. The displacement between the two shocks in this case will be determined by the standoff distance of the bow shock from the front side of the obstacle. For high Mach number flows, this standoff distance will be significantly smaller than the cloud (see Fig. 1 of Raga and Böhm 1985). Therefore, the displacement between the shocked wind material and shocked obstacle material can be significantly smaller than the size of the obstacle itself. Thus, even for a cloudlet which is itself resolved, the displacement between the bow shock emission and cloud shock emission could still be unresolved. It is therefore plausible that a shocked cloudlet may exhibit little or no observable offset between the position of its peak $H\alpha$, $[S\ II]$ emission and the position of its peak H_2 emission.

In the cloudlet case just discussed, the dynamic pressure of the flow acts to move the postshock material away downstream. This does not occur in the case of a flow terminus geometry, where shocked jet material and shocked wind material accumulate in geometrically closed region. The terminal jet shock will occur where the jet strikes this accumulated material—a location distinctly separate from the bow shock in the ambient medium. The visibility of this terminal jet shock has been discussed by Hartigan (1989). The separation of the two shocks in this scenario should be significantly larger the shock separation in the cloudlet scenario—probably comparable in size to the width of the jet.

The two separate $[S\ II]$ peaks in HH 7, one of which does not have an H_2 counterpart, suggest that two distinct shocks are indeed present in HH 7. The absence of HH objects to the east of HH 7, coupled with the object's bow shape (concave open to SVS 13), makes it clear that HH 7 is the eastern terminus of the outflow from SVS 13. Using the flow terminus model, we identify the western $[S\ II]$ peak in HH 7 as the location of the terminal jet shock. The eastern $[S\ II]$ peak (and the peak H_2 emission) then correspond to the bow shock in the ambient molecular medium. Hartigan, Curiel, and Raymond (1989) have also discussed this interpretation. This model naturally accounts for the lack of a western H_2 peak: the terminal jet shock is occurring entirely within wind material where very little H_2 is present. The model is also supported by new imaging spectroscopy of HH 7–11 (Stapel Feldt, Trauger, and Scoville 1991) which shows that much of the intensity of HH

7's western [S II] peak originates from a -100 km s^{-1} high velocity component not present in eastern HH 7.

There is both kinematic and spatial evidence for separate H_2 and [S II] formation regions in the bow shock on the eastern edges of HH 7. First are the radial velocity data: Carr (1990) and Zinnecker *et al.* (1989) find much lower H_2 velocities than Stapelfeldt, Trauger, and Scoville (1991) and Solf and Böhm (1987) find for [S II] and $\text{H}\alpha$ in HH 7. Second, as we reported above, the H_2 peak is more broadly extended perpendicular to the flow direction than the [S II] peak that it spatially coincides with. Greater extinction at the periphery of HH 7 does not account for this, as the infrared [Fe II] distribution essentially matches the optical [S II] distribution. Excitation gradients caused by the variation in effective shock velocity over the bow shock surface are probably not large enough to account for the observed peak shape variations. A very plausible explanation for the observations is that the region of bright H_2 emission is located *exterior* to the more axially concentrated [S II] emission.

Separate H_2 and [S II] emission regions are expected if the HH 7 bow shock takes the form of a J shock with a magnetic precursor, as proposed by Hartigan, Curiel, and Raymond (1989). This model predicts that the H_2 emission forms where the shock precursor heats and accelerates the preshock molecular cloud material; with a flow terminus bow shock geometry, the precursor H_2 emission will form in a shell *exterior* to the region of [S II] emission from the J shock itself. An alternate molecular emission scenario predicts that the H_2 emission will form in the cooling zone behind a shock, perhaps with a significant contribution from molecule re-formation processes (Hollenbach and McKee 1989). In a flow terminus bow shock geometry, this scenario would have the H_2 emission forming in a shell *interior* to the [S II] emission in the postshock cooling zone. We see no obvious way for such interior postshock H_2 emission to be more broadly extended from the bow shock axis than [S II] emission, as our observations show is the case in eastern HH 7. It seems straightforward, however, for an exterior shell of H_2 emission to appear more broadly extended from the bow shock axis than an interior shell of [S II] emission. On these geometrical grounds it therefore appears likely that the brightest H_2 emission in HH 7 is excited by a magnetic precursor.

In the case shown in Figure 4a, which we apply to HH 7, the jet is in rough pressure equilibrium with the surrounding material (region 1). Region 1, in turn, is probably close to pressure equilibrium with the ambient material (region 0). The region between the jet shock and the shock driven into the ambient material (region 2) must satisfy $p_2 \approx \rho_s v_s^2$, so $p_2 \gg p_1$ and $p_2 \gg p_0$. Region 2 is filled with shocked jet and ambient material at high pressure, which then flows out into region 1. It is possible (but not necessarily the case) that there is a shock transition between region 2 and region 1 arising from the effective venturi formed by the jet and the opening walls of the cavity.

It does not have to be the case that $p_1 = p_0$. If the cavity around the jet is mostly enclosed, then the energy input from the jet will pressurize the cavity. If $p_1 > p_0$, then weak shocks will be driven into the cavity walls. Such shocks could be the source of the diffuse ubiquitous H_2 emission in HH 7–11. It should also be noted that there will be a velocity shear across the contact discontinuity between shocked jet and ambient material. The shocked jet material will be primarily flowing along the discontinuity on its way out of region 2; at the same

time, ambient material is shocked and enters region 2. The contact discontinuity will be Kelvin-Helmholtz unstable and mixing will occur. Thus, distinctions between emission from regions of shocked jet material and regions of shocked ambient material may be largely artificial in some cases. In particular, mixing of molecular material not dissociated by the bow shock with the warm atomic gas in region 2 could be a significant additional source of molecular emission. This mixing could also significantly complicate interpretation of high resolution spectroscopy of HH objects.

Some of the atomic emission extended perpendicular to the flow in HH 7 could also be due to shocked jet material. If material remains in region 2 for a time which is less than or comparable to the time scale for radiative cooling and recombination of the emitting species, then the emissivity will be high throughout this region of high pressure. In this case, the spatial extent of the emission from region 2 would be similar to the spatial extent of bow shock emission because the pressure in region 2 drives the bow shock.

The nature of HH 8, HH 9, and HH 10 is not as easy to discern as that of HH 7. Rudolph and Welch (1988) interpreted the zero-velocity HCO^+ peaks just to the east of these objects as shocked cloudlet emission. For the purpose of discussion, let us assume that HH 8, HH 9, and HH 10 are shocked molecular cloudlets in a neutral wind. If so, we would expect the cloudlet shock to produce both bright H_2 emission and the HCO^+ . Our observations show that the peak H_2 emission in HH 8, HH 9, and HH 10 is nearly coincident with the optical [S II] peaks. This means that the H_2 peaks are *also* located upstream (by $3''$ – $8''$) of the HCO^+ peaks. A naive cloudlet model might not have expected the H_2 and HCO^+ peaks to be spatially separated. In the context of the cloudlet model, this observation can be best understood if the H_2 emission forms in warm postshock gas and the HCO^+ emission arises in the cold preshock medium. The HCO^+ emission is then most likely excited by a radiative or magnetic precursor of the cloudlet shock, by weak shocks acting on the rear of the cloudlet, or by the simple high density of the undisturbed cloudlet material.

We do not feel that Rudolph and Welch's (1988) original suggestion, that the HCO^+ emission arises in dense gas compressed by the cloudlet shock, can be easily reconciled to the observed spatial relationship between the HCO^+ and H_2 peaks. If a single cloudlet shock was responsible for both the HCO^+ emission (by compressing the gas above the HCO^+ $J = 1-0$ critical density) and the H_2 emission (by heating the H_2 to near 2000 K), then the shock must be located just to the east of the HCO^+ peaks. This implies that the HCO^+ emission region must lie closer to the shock than the H_2 formation region. For radiative shocks, this assumption further implies that the HCO^+ emission should form in a region of higher temperature than the region of H_2 emission. However, this cannot be the case: because the observed HCO^+ emission originates in a level only 4 K above the molecular ground state, we expect essentially no $J = 1-0$ HCO^+ emission to form in regions as warm (2000 K) as those where $2 \mu\text{m}$ H_2 emission originates. We therefore conclude that the HCO^+ and H_2 emission in HH 8, HH 9, and HH 10 cannot *both* be excited in the material that has completely passed through a single cloudlet shock.

An alternative explanation that would still allow HCO^+ formation in the shocked gas is the following: if the cloudlet shock was of very low velocity (a few km s^{-1}), it could potentially produce the HCO^+ peaks via compression without

producing detectable H_2 emission. In this case, the weak cloudlet shock would be located just to the east of the HCO^+ peaks. However, another mechanism is needed in this case to explain how the emission from warm H_2 is formed several arcseconds to the west. It may be that the entrainment of cloudlet material by the neutral wind can produce the H_2 emission on the cloudlet's upstream surface.

The lack of a significant H_2 -[S II] offset in HH 8, HH 9, and HH 10 is not a problem for a cloudlet model of these objects. As discussed earlier in this section, the spatial separation between wind and cloudlet shocks can be unresolved even for a resolved cloudlet. Morphology is another issue. In H_2 and [S II], neither HH 8 or HH 10 has the appearance of an idealized cloudlet (Fig. 4b): there is no identifiable bow shock structure, and axial symmetry is lacking. However, we believe that a nonideal cloudlet is still a viable model for HH 8 and HH 10. A flow obstacle that has an irregular nonspherical shape, or one which is partially embedded in the outflow cavity wall can break the symmetry in Figure 4b. Regardless of the shape of the obstacle, we expect that both the wind and obstacle material will be shocked and produce emission. If the wind is neutral, the shocked wind material may be evident as a bright [S II], $H\alpha$ emission knot that has no H_2 counterpart. Such peaks are present in both HH 8 and HH 10: in HH 8, at the northwestern tip; and in HH 10, near the geometric center of the object. In both cases, an $H\alpha$ - H_2 comparison reveals these peaks most clearly (see Hartigan, Curiel, and Raymond 1989). The presence of these shocked wind peaks adjacent to the H_2 peaks in HH 8 and HH 10 suggests that a flow obstacle model is a viable explanation for these objects.

HH 11 does not seem to fit either of the two pictures depicted in Figure 4. A nearby HCO^+ cloudlet appears to be associated with HH 11b, not HH 11 itself; the line profiles do not include zero velocity (Stapel Feldt, Trauger, and Scoville 1991; Solf and Böhm 1987); and there is no H_2 emission. The lack of molecular emission from HH 11 suggests one of two situations: either the material being shocked is not molecular gas, or the shock itself is strong enough to dissociate molecules before any emission is excited.

The absence of molecular emission also indicates that no molecule formation is occurring in a postshock cooling zone at this location. This may not be a strong test of model predictions of molecule formation in shocks, however, since the object may be too young for molecular formation to be important yet. From the models by Hollenbach and McKee (1989), the column depth required for significant H_2 emission from the zone of molecule formation is $\sim 3 \times 10^{20} \text{ cm}^{-2}$. For $v_s = 50 \text{ km s}^{-1}$ and $n_0 = 10^3 \text{ cm}^{-3}$, it takes about 2000 yr to accumulate this column depth. This is long compared to the dynamic time scale of 300 yr inferred from the proper motion of the object and the distance to the source (Herbig and Jones 1983).

The essential features of Figure 4b are similar to those of Figure 4a, with shocked jet material confined for a time in the high-pressure region 2 between the jet and cloud shocks. As with Figure 4a, $p_2 \gg p_0$ and $p_2 \gg p_1$, and the possibility exists for a shock transition between region 2 and region 1. The time scale for confinement of shocked jet material in region 2 will be shorter for Figure 4b. As shocked material escapes from region 2, its emissivity will drop abruptly and dramatically. This is due to the combined effects of lower density and mechanical cooling that occur as a result of the expansion. For example, the Boltzmann factor for the 2D level of S II changes from 0.13 to 0.02 between 10,000 and 5000 K. This phenomenon of

incomplete cooling and recombination is discussed below in the case of HH 12E.

b) HH 12

HH 12 is one of the more extended complexes of Herbig-Haro objects, measuring $30'' \times 50''$ in size. It is located in L1450 approximately $5'$ NW of HH 7-11. The optical emission knots of HH 12 are blueshifted with respect to the ambient cloud and are coincident with the blue lobe of a CO outflow (Edwards and Snell 1983). Unlike HH 7-11, the outflow source has not been positively identified. The infrared source SVS 12, located $20''$ to the east of HH 12, has been suggested as the exciting star (Strom, Vrba, and Strom 1976; Edwards and Snell 1983; Cohen and Schwartz 1983). However, the proper motions of HH 12B and HH 12F are directed toward the north (Herbig and Jones 1983), roughly perpendicular to the direction of SVS 12. It is difficult to reconcile this result with an outflow from SVS 12. Strom, and Stocke (1983) suggested that a star $2'$ to the south is the outflow source, but additional observations failed to confirm this (Strom *et al.* 1986). New arguments supporting a case for SVS 12 as the HH 12 exciting star are presented by Stapelfeldt (1991) and Stapelfeldt, Trauger, and Scoville (1991) on the basis of the local molecular gas distribution and [S II] radial velocities. On the basis of these, we adopt SVS 12 as the exciting star in the discussion below.

The near-infrared luminosity of HH 12 is predominantly line emission; continuum images (such as $2.19 \mu\text{m}$; Fig. 5b) show no significant emission. The brightest source in this field is SVS 12 and its reflection nebula, which are discussed below.

i) [Fe II]

As was the case for HH 7-11, all of the HH 12 optical emission knots are also present in [Fe II] (see Fig. 5d). There are no additional emission features seen [Fe II] $1.64 \mu\text{m}$ which were not already apparent in the optical emission line morphology. To the limits of our resolution and image registration, the [Fe II] and [S II] emission peaks are spatially coincident. HH 12B shows the highest [Fe II] surface brightness within HH 12.

HH 12E is an exception to the generally good agreement we see between [S II] and [Fe II]. At this location, [S II]/[Fe II] is a factor of 7 higher than typical in other nearby knots. This is difficult to interpret using steady flow shock models, which indicate that [S II]/[Fe II] should be fairly constant for shock velocities in the relevant range (Hollenbach and McKee 1989). A deficit of [Fe II] emission from the shocked wind material can be explained by incomplete cooling of the postshock gas. This idea has been used to explain similar discrepancies between observations and shock models in supernova remnants (see Raymond *et al.* 1988 and references therein). The second ionization potentials for S and Fe are quite different (23.3 eV vs. 16.2 eV). Assuming a shock velocity adequate to ionize S, there should be a significant region in the cooling and recombining flow behind the shock where Fe is predominantly Fe^{+2} while S is predominantly S^+ . If too little material has passed through the shock for the Fe^+ zone to form, or if the geometry of the flow is such that material behind the shock never cools enough to produce much [Fe II] emission, then the [S II]/[Fe II] ratio can become larger. The geometry of HH 12E appears consistent with a small cloudlet (Fig. 4b) or a protrusion into the flow, and it is likely that shocked wind material is confined to the zone between the bow shock and

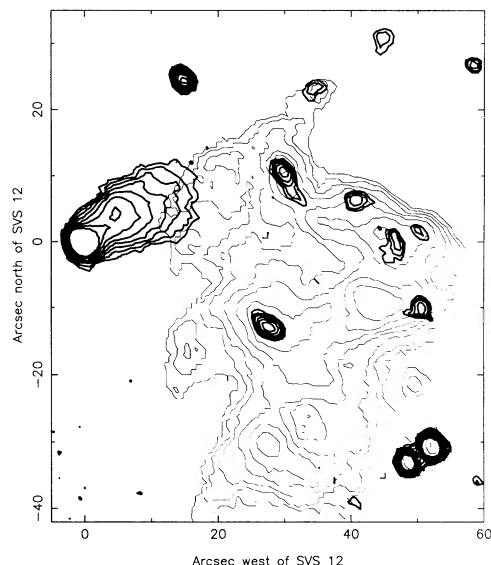


FIG. 6.—An overlay of two contour plots of the emission from HH 12. The dark contours represent H_2 $Q(3)$ emission; the light contours represent the 6717 \AA $[S \text{ II}]$ emission. The contour interval is a factor of $\sqrt{2}$.

cloudlet shock for a short time only. In this interpretation, the region of molecular formation would also be absent behind the bowshock, so the H_2 emission from HH 12E must originate from a separate shock in the cloudlet material. This scenario admittedly requires that the shocked flow in HH 12E somehow be “disrupted” at a fairly special place; however, we point out that of the objects observed, HH 12E is the only one with a significantly anomalous $[S \text{ II}]/[Fe]$ ratio. Model calculations showing the $[S \text{ II}]$ and $[Fe \text{ II}]$ emission as a function of column depth would enable a more quantitative analysis of HH 12E.

ii) H_2

Figure 6 shows the spatial relationship between the $[S \text{ II}]$ and H_2 emission in HH 12. The morphology of the H_2 emission is remarkably different from the optical emission lines. The $Q(3)$ emission (Fig. 5a) in knots B, Cw, E and G is coincident with the $[S \text{ II}]$ and $[Fe \text{ II}]$ emission (Fig. 5e). Significant offsets are evident, however, the cases of knots C, D, and F. Peak H_2 $Q(3)$ emission occurs $2''$ west of the $[S \text{ II}]$ peak in knot C. The H_2 counterpart of knot D (referred to here as knot Dm) appears $8''$ west of its optical counterpart (Di). Faint $Q(3)$ emission associated with knot F lies $8''$ SW of the corresponding optical emission.

All three of these H_2 – $[S \text{ II}]$ offset vectors point back toward SVS 12. In addition, $Q(3)$ knots we call Cn and Cw appear north and west of optical knot C. Small $[S \text{ II}]$ knots coincide with Cn and Cw. Finally, there is a knot of $Q(3)$ emission, colinear with SVS 12 and optical knot G. This H_2 feature has no optical counterpart; we designate it HH 12H. The morphology of the $S(1)$ emission image (not shown here) is very similar to the $Q(3)$ emission in Figure 3a. The 2–1 $S(1)$ emission was detected only in knot E and the peak $v = 1\text{--}0/2\text{--}1$ ratio is 16.

In HH 12, the molecular hydrogen emission tends to be distributed in discrete clumps; the optical emission includes and extends between these clumps. This is a real effect and is not due to infrared sensitivity limitations: the $[S \text{ II}]$ intensity between knots D and E is about a factor of 3 reduced from the value on the peaks. Limits for the H_2 emission between these

knots show that the knot/interknot intensity ratio here is greater than 10. This result suggests that HH 12's H_2 emission is predominantly formed in clumps of ambient medium shocked by the pressure of the stellar wind.

HH 12 has the appearance of the termination of a wide opening angle conical flow from the east against the approximately N–S boundary of a molecular cloud. The morphological properties of HH 12 can be interpreted under this assumption as follows: The easternmost knots in the system are either small cloudlets (E, G) or dense protrusions into the flow (B) that have not yet been eroded away. There is no measurable displacement between the molecular and atomic emission in these knots; as was discussed in the previous section, a cloudlet geometry is consistent with this observation. The diffuse atomic emission (between knots B–C; D–E; E–F) arises from shocked wind material that is ubiquitous throughout these regions. The emission along the western edges of HH 12 represents the termination of the flow, and here offsets are found between the molecular and atomic emission. Knots Cn, Cw, and Dm show both H_2 and $[S \text{ II}]$ emission from the shocked ambient medium. In knot Di and in the eastern side of knot C, only shocked atomic material is present. Here, as with HH 7, enough material “piles up” for the shocked wind material to be offset an observable distance upstream from the shocked ambient material.

iii) Continuum

The bright infrared continuum source in this field is SVS 12 and its reflection nebula. The star itself is located at the extreme southeastern tip of the near-infrared reflection nebula; both the star and the nebula are highly obscured at optical wavelengths (Fig. 5e). The axis of the nebula is aligned well with the line formed by SVS 12, HH 12G, and HH 12H. This appears to bolster the suggestion made by Cohen and Jones (1987), that an outflow from SVS 12 is responsible for the shock excitation of HH 12G and HH 12H (see also Garden *et al.* 1990). If SVS 12 is the exciting star for all of HH 12, then the outflow must take the form of a broad cone (half angle $\sim 40^\circ$) to encompass all of HH 12. In this view, the axis of the reflection nebula forms the NE boundary of the cone; the SE boundary follows the SVS 12–HH 12F line.

The stellar continuum source SVS 12 has some striking characteristics. Very strong circumstellar extinction is evident from a comparison of the K and J band images (Figs. 5a and 5c). The star is hardly visible at J ; we find $(m_J - m_K) \geq 6$ mag. The reflection nebula is substantially less reddened: $(m_J - m_K) = 3$ mag. Embedded objects with extremely red $J - K$ colors have been studied by Myers *et al.* (1987), who suggested that these are very young stars ($T_{\text{eff}} \sim 3000 \text{ K}$) extinguished by 20–30 mag. The strong localized reddening indicates that SVS 12 may possess a substantial circumstellar disk.

The J band image (Fig. 5c) shows several locations of significant emission which are not present in any of our narrow-band continuum images (such as the $2.19 \mu\text{m}$ image shown in Fig. 4b). The J features are spatially coincident with the HH 12 optical knots B, C, D, E, and F, and they exhibit similar morphology. This close association with known emission-line regions, coupled with the observed lack of near-infrared continuum emission from those regions, strongly argues that we are observing line emission in the J image. A definite source of line emission in the J band ($1.15\text{--}1.40 \mu\text{m}$) is the $1.257 \mu\text{m}$ $[Fe \text{ II}]$ line which arises from the same upper state and has nearly equal transition probability as the $1.644 \mu\text{m}$ line. This is

undoubtedly the primary source of the J band emission seen. This cannot be the whole explanation, however, since knot E should be relatively faint if $[\text{Fe II}]$ $1.257\ \mu\text{m}$ emission dominated its J flux. Paschen- β ($1.281\ \mu\text{m}$) may account for the remaining emission from knot E.

c) HH 34

HH 34 is located in the L1641 cloud in Orion. Mundt (1986) and Reipurth *et al.* (1986) independently discovered a highly collimated jet pointing toward HH 34 from an optically faint star $110''$ to the north. They realized that HH 34 itself is probably the "working surface" of this jet, a bow shock formed where the jet actively carves out a cavity in the ambient medium. A symmetrically placed bow shock on the northern side of the star was found by Bührke, Mundt, and Ray (1988). They designated the northern bow shock as HH 34N and renamed the original object HH 34S. One of the intriguing aspects of this star-jet-shock system is the apparent lack of a jet directed toward HH 34N. Three fields were observed by us: the star/jet, the southern bow shock, and the northern bow shock. Figure 7 shows our infrared images of the star/jet field.

i) $[\text{Fe II}]$

The HH 34 jet is the only line emission feature in the $[\text{Fe II}]$ image, Figure 7d. It is of interest to compare the $[\text{Fe II}]$ spatial structure of the jet with the known $[\text{S II}]$ structure, and this comparison is shown in Figure 8. The $[\text{Fe II}]$ profile of the jet is very similar to the $[\text{S II}]$ profile; the only prominent difference is the slightly lower spatial resolution of the $[\text{Fe II}]$ data. The similarity of the optical and near-infrared ionized gas emission line structure suggests that the lack of emission between the star and the bright knots of the jet is not due to local extinction. There is also strong $[\text{Fe II}]$ line emission from the position of the star: in our filters, the $1.64\ \mu\text{m}$ flux density is $5\ \text{mJy}$ and the $1.57\ \mu\text{m}$ flux density is $2\ \text{mJy}$. Assuming that no other lines fall in our filter bandpass and that the $1.64\ \mu\text{m}$ $[\text{Fe II}]$ linewidth is $100\ \text{km s}^{-1}$, the $1.64\ \mu\text{m}$ $[\text{Fe II}]$ emission line intensity must exceed the stellar continuum by a factor of 20.

Figure 7d shows no evidence of a counterjet in $[\text{Fe II}]$ to the north of the HH 34 star. If the counterjet were as intrinsically bright as the southern jet, then it would have to be extinguished by at least 3 mag at $1.64\ \mu\text{m}$ to escape our detection. This corresponds to 14 mag at $[\text{S II}]$ $6717\ \text{\AA}$. There are two reasons that such a large optical extinction seems implausible in the region where a counterjet is expected. First is the $H\alpha$ flux ratio of 0.1 we measure between HH 34N and HH 34S. Assuming these two objects to be of comparable intrinsic brightness, this observation implies that the extinction toward HH 34N exceeds that toward HH 34S by only $A_{H\alpha} = 2.5$ mag. Second, ^{13}CO millimeter interferometry of the HH 34 star region (Stapelfeldt 1991) shows that the dense circumstellar gas is confined to an area within $10''$ of the HH 34 star. The spatial extent of this gas is therefore insufficient to obscure a northern jet of length equal to the southern jet ($\sim 20''$). We therefore conclude that the primary reason for our nondetection of a northern jet is its intrinsic faintness in $[\text{Fe II}]$ relative to the southern jet. The collimated flow to the north is therefore encountering little lateral confinement (and thus no shock interactions with the ambient medium) as it makes its way to the bow shock at HH 34N. A remaining speculative possibility is that the jet source mechanism is somehow intrinsically asymmetric in nature.

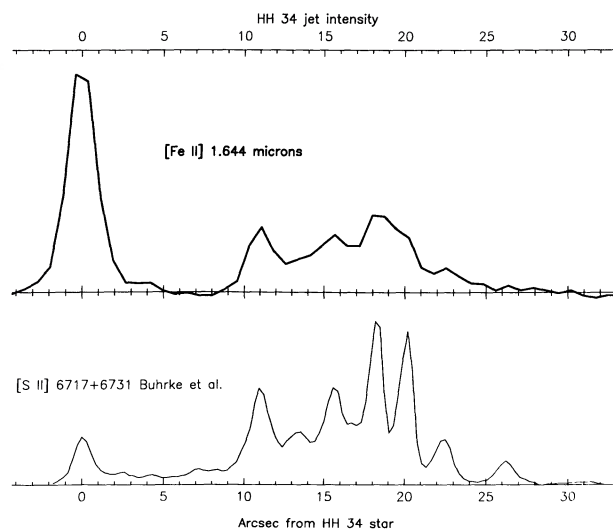


FIG. 8.—Comparison of the $[\text{Fe II}]$ $1.64\ \mu\text{m}$ and $[\text{S II}]$ $6717+6731\ \text{\AA}$ emission structure in the HH 34 jet. A swath $6''$ wide was used to bin the infrared data. Continuum subtraction was performed for the $[\text{Fe II}]$ curve. The $[\text{S II}]$ tracing is taken from Fig. 4 of Bührke *et al.* (1988).

HH 34S is only a weak source of $1.64\ \mu\text{m}$ emission in comparison to the jet (image not presented here). The $[\text{Fe II}]$ again appears to follow the optical $[\text{S II}]$ distribution, but the details cannot be precisely determined because of image alignment uncertainties: there is no reference star in this field visible at both optical and infrared wavelengths. The bow shock $[\text{Fe II}]$ flux may be weak because only a single shock is present here; in the jet, multiple oblique shocks allow many $[\text{Fe II}]$ emission regions. HH 34N was not detected in our $[\text{Fe II}]$ observations. This non-detection requires that the total $[\text{Fe II}]$ flux from HH 34N must be at least a factor of 3 less than the flux from HH 34S. The observed optical brightness ratio of these objects (a factor of 10) easily accounts for the HH 34N $[\text{Fe II}]$ non-detection without any effects of extinction.

ii) H_2

Molecular hydrogen emission was not detected in any of the three HH 34 fields. The absence of H_2 emission from both bow shocks may reflect the prevalence of relatively low density molecular gas in the environs of this object. The widespread $H\alpha$ emission in this field suggests a significant atomic component to the local ambient medium. If the ambient medium H_2 volume densities were below $10^3\ \text{cm}^{-3}$, the emissivity of the H_2 shocks would be low enough to render them unobservable.

The lack of H_2 emission from the HH 34 jet suggests that the jet may not contain any molecular material. The very low excitation spectrum of the jet is indicative of a physical environment which should be ideal for producing H_2 emission, yet none is observed. It may be that the jet density is also too low to produce observable H_2 emission; future observations with higher sensitivity may be able to provide definitive limits on the molecular fraction of the jet material.

iii) Continuum

Along with the HH 34 star near the center, two other stars in this field are obscured in the optical (see Figs. 1a–1c). One is $20''$ to the west and is located at the position of optical reflection nebulosity; the other is in the upper left of the images, and corresponds to Cohen and Schwartz (1983)'s HH 34 IRS 5.

Our position for IRS 5 is $\alpha = 05^{\text{h}}33^{\text{m}}04^{\text{s}}.8$ $\delta = -06^{\circ}28'26''$ (1950), or $5''$ NNE of Cohen and Schwartz's position. IRS 5 illuminates two patches of reflection nebosity to its south and west. Faint jet emission is apparent in the J image, probably originating from the $[\text{Fe II}]$ $1.257 \mu\text{m}$ line.

An interesting feature of the continuum images is the diffuse emission north of the HH 34 star. The emission is brighter at longer wavelengths, and in the K image (Fig. 7c) appears to be concentrated around a distinct source. Recent millimeter-wave interferometry of the HH 34 star (Stapelfeldt 1991) reveals extended $^{13}\text{CO } J = 1-0$ emission in this region and the suggestion of a condensation at the position of the spot. It is unclear if this region is solely reflection nebosity or if it also contains a separate, highly obscured stellar source. K band polarization measurements and high-resolution $5 \mu\text{m}$ images of this field would be very useful for resolving this uncertainty.

d) Why the 1.64 Micron Emission Must Be $[\text{Fe II}]$

We have confidence that the emission detected in our $1.64 \mu\text{m}$ filter is in fact $[\text{Fe II}]$ emission. First, there is no doubt that we have detected line emission at $1.64 \mu\text{m}$: none of the HH objects we have discussed were detected in our 3% bandwidth $1.57 \mu\text{m}$ images. In the HH 34 jet, $1.64 \mu\text{m}$ $[\text{Fe II}]$ line emission is expected because this object is known to be a strong emitter in the 8617 \AA $[\text{Fe II}]$ line (Reipurth *et al.* 1986). Furthermore, the fact that no H_2 $1-0$ $S(1)$ or $1-0$ $Q(3)$ line emission is detected in the jet makes it very unlikely that higher level H_2 lines [such as $3-1$ $O(7)$ and $6-4$ $Q(5)$] could be present at the intensity required to account for the observed $1.64 \mu\text{m}$ emission (see Black and van Dishoeck 1987). In HH 7-11 and HH 12, the observed distribution of $1.64 \mu\text{m}$ emission correlates well with 6717 \AA $[\text{S II}]$ emission, but does not follow the H_2 emission: crucial examples of this are found in western HH 7, HH 11, and HH 12D, where $[\text{Fe II}]$ peaks appear coincident with $[\text{S II}]$ and no H_2 emission peaks are present. Last, our wide-band J images of HH 12 and the HH 34 jet show faint but definite signs of the HH objects, as expected from the presence of the $1.26 \mu\text{m}$ $[\text{Fe II}]$ line in the filter bandpass. Neither object is known to possess a significant continuum component in the optical or near-infrared. We therefore conclude that we have a strong basis for associating our observed $1.64 \mu\text{m}$ emission with $[\text{Fe II}]$.

IV. CONCLUSIONS

The principal results of our high-resolution, near-infrared imaging of HH objects are as follows:

1. $1.64 \mu\text{m}$ $[\text{Fe II}]$ emission has been detected in HH 7-11, HH 12, and HH 34. Its morphology resembles that of the red $[\text{S II}]$ lines. The intensity of $[\text{Fe II}]$ is typically 20% that of H_2 $1-0$ $S(1)$. This line should be an excellent tracer of shocked ionized gas in highly obscured regions, and along with $1.26 \mu\text{m}$ $[\text{Fe II}]$ measurements will allow an accurate determination of the local extinction. Variations in the $[\text{Fe II}]/[\text{S II}]$ ratio within the HH object complexes we studied are generally small except in HH 12E, where the ratio is down by a factor of 7 relative to other knots in the object. At this location, incomplete cooling and recombination in the flow behind the shock can account for the exceptionally weak $[\text{Fe II}]$.

2. Extinction appears to be unimportant in determining the morphology of these HH object systems. Standard extinction curves predict that the extinction in magnitudes at the $1.64 \mu\text{m}$

$[\text{Fe II}]$ line is nearly 5 times less than that at the 6717 \AA $[\text{S II}]$ line yet no new regions of shock ionized gas were found at $1.64 \mu\text{m}$. In addition, the H_2 $Q(3)$ and $S(1)$ line images appear very similar. Thus, the distribution of optical and near-infrared line emission in these HH objects is dictated by hydrodynamic conditions rather than the distribution of absorbing dust. The outflow source stars themselves are highly obscured, however, which indicates the presence of substantial circumstellar dust.

3. No near-infrared continuum emission was detected from any of the HH objects, implying that these regions do not contain embedded stars. An infrared reflection nebula, possibly containing a new point source, has been discovered north of the HH 34 exciting star.

4. At positions where the flow terminates against a large obstacle (HH 7 and the western portion of HH 12), there are significant offsets between the shocked flow material and the shocked ambient medium. At these locations the geometry is such that significant amounts of material can "pile up" between the jet shock and the shock driven into ambient material, leading to an observable displacement between the two shocks. At locations where a flow is interacting with small clumps of ambient material (HH 9, HH 12E, etc.), the wind shock and ambient medium shock are generally coincident (within the limits of our resolution). At these locations the standoff distance between the wind and cloud shocks is expected to be smaller. The data fit an interpretation in which shocked jet/wind material is a source of atomic emission only, whereas shocked ambient material produces both molecular and atomic emission.

5. We have observed a significant difference between the shapes of the H_2 and $[\text{S II}]$ emission peaks on the east side of HH 7. The broader H_2 peak suggests that bright molecular emission is formed in a region *exterior* to the $[\text{S II}]$ emission, as expected if the H_2 emission arises within a magnetic precursor.

The work described in this paper would not have been possible without the many years of dedicated work by JPL's Gary Bailey in developing infrared arrays for astronomical use. Gary died in January of this year. His insight into the practical applications of arrays, his trenchant wit and unwavering dedication to the progress of science will all be sorely missed by his colleagues.

It is a pleasure to thank the staff of Palomar Observatory for their assistance with the observations. The HIRIS project at JPL made the detector available; Richard Lucinio (Caltech) was helpful in preparing the camera for use. We thank John Trauger (JPL) for the use of the WF/PC II computing facilities and his $[\text{S II}]$ filter. Deborah Padgett and Jim McCarthy provided valuable assistance to the optical observing and data reduction; Brian Gordon and Dwight Moody (JPL) assisted in the production of the images; and Jorden Woods integrated and improved the data reduction software. We acknowledge helpful discussions with John Carr, James R. Graham, Dave Hollenbach, John Raymond, and Dave van Buren. Thanks are also due to Pat Hartigan, who as referee provided comments that helped improve the discussion sections. The camera construction was supported by a grant from the Caltech President's Fund, with continuing funding from NASA grant RTOP 100-44-24-10. N. Z. S. acknowledges support from NSF grant AST 87-14405, and K. R. S. acknowledges the support of a NASA fellowship.

REFERENCES

- Beichman, C. A., Hester, J. J., and Gautier, T. N. 1991, in preparation.
- Black, J. H., and van Dishoeck, E. F. 1987, *Ap. J.*, **322**, 412.
- Bührke, T., Mundt, R., and Ray, T. P. 1988, *Astr. Ap.*, **200**, 99.
- Burton, M. G., Brand, P., Geballe, T. R., and Webster, A. S. 1988, *M.N.R.A.S.*, **236**, 409.
- Cohen, M., and Jones, B. F. 1987, *Ap. J.*, **321**, 846.
- Cohen, M., and Schwartz, R. D. 1983, *Ap. J.*, **265**, 877.
- Delbouille, L., Roland, G., Brault, J., and Testerman, L. 1981, *Photometric Atlas of the Solar Spectrum from 1850 to 10000 cm⁻²* (Tucson AZ: Kitt Peak National Observatory).
- Edwards, S., and Snell, R. L. 1983, *Ap. J.*, **270**, 605.
- Elias, J. H., Frogel, J. A., Matthews, K., and Neugebauer, G. 1982, *A.J.*, **87**, 1029.
- Garden, R. P., Russell, A. P. G., and Burton, M. G. 1990, *Ap. J.*, **354**, 232.
- Graham, J. R., Wright, G. S., and Longmore, A. J. 1987, *Ap. J.*, **313**, 847.
- Hartigan, P. 1989, *Ap. J.*, **339**, 987.
- Hartigan, P., Curiel, S., and Raymond, J. 1989, *Ap. J. (Letters)*, **347**, L31.
- Herbig, G. H., and Jones, B. F. 1983, *A.J.*, **88**, 1040.
- Herbig, G. H., and Terndrup, D. M. 1986, *Ap. J.*, **307**, 609.
- Hollenbach, D., and McKee, C. F. 1989, *Ap. J.*, **342**, 306.
- Lane, A. P. 1989, in *Low Mass Star Formation and Pre-Main Sequence Objects* (ESO Conf. Proc. 33), ed. B. Reipurth (Garching: ESO), p. 33.
- Lizano, S., Heiles, J., Rodriguez, L., Koo, B., Shu, F. H., Hasegawa, T., Hayashi, S., and Mirabel, I. F. 1988, *Ap. J.*, **328**, 763.
- Mundt, R. 1986, *Canadian J. Phys.*, **64**, 407.
- Mundt, R., Brugel, E. W., and Bührke, T. 1987, *Ap. J.*, **319**, 275.
- Myers, P. C., Fuller, G. A., Mathieu, R. D., Beichman, C. A., Benson, P. J., Schild, R. E., and Emerson, J. P. 1987, *Ap. J.*, **319**, 340.
- Norman, C. A., and Silk, J. 1979, *Ap. J.*, **228**, 197.
- Raga, A. C., and Böhm, K. H. 1985, *Ap. J. Suppl.*, **58**, 201.
- Raymond, J. C., Hester, J. J., Cox, D. P., Blair, W. P., Fesen, R. A., and Gull, T. R. 1988, *Ap. J.*, **324**, 869.
- Reipurth, B., Bally, J., Graham, J. A., Lane, A. P., and Zealey, W. J. 1986, *Astr. Ap.*, **164**, 51.
- Rudolph, A., and Welch, W. J. 1988, *Ap. J. (Letters)*, **326**, L31.
- Schwartz, R. D. 1978, *Ap. J.*, **223**, 884.
- . 1983, *Ann. Rev. Astr. Ap.*, **21**, 209.
- Schwartz, R. D., Cohen, M., and Williams, P. M. 1987, *Ap. J.*, **322**, 403.
- Schwartz, R. D., Williams, P. M., Cohen, M., and Jennings, D. G. 1988, *Ap. J. (Letters)*, **334**, L99.
- Snell, R. L., and Edwards, S. 1981, *Ap. J.*, **251**, 103.
- Solf, J., and Böhm, K. H. 1987, *A.J.*, **93**, 1172.
- Stapelfeldt, K. R. 1991, in preparation.
- Stapelfeldt, K. R., Trauger, J. T., and Scoville, N. Z. 1991, in preparation.
- Strom, K. M., Strom, S. E., and Stocke, J. 1983, *Ap. J. (Letters)*, **271**, L23.
- Strom, K. M., Strom, S. E., Wolff, S. C., Morgan, J., and Wenz, M. 1986, *Ap. J. Suppl.*, **62**, 39.
- Strom, S. E., Vrba, F. J., and Strom, K. M. 1976, *A.J.*, **81**, 314.
- Turner, J., Kirby-Docken, K., and Dalgarno, A. 1977, *Ap. J. Suppl.*, **35**, 281.
- Zinnecker, H., Mundt, R., Geballe, T. R., and Zealey, W. J. 1989, *Ap. J.*, **342**, 337.

CHARLES A. BEICHMAN: Institute for Advanced Study, Princeton, NJ 08540

THOMAS N. GAUTIER III and J. JEFF HESTER: California Institute of Technology, MS 100-22 IPAC, Pasadena, CA 91125

NICHOLAS Z. SCOVILLE and KARL R. STAPELFELDT: Mail Code 105-24, California Institute of Technology, Pasadena, CA 91125